Journal of Biomedical Optics

BiomedicalOptics.SPIEDigitalLibrary.org

Labeling of HeLa cells using $ZrO_2:Yb^{3+}$-Er^{3+} nanoparticles with upconversion emission

Andrea Ceja-Fdez
Tzarara López-Luke
Jorge Oliva
Juan Vivero-Escoto
Ana Lilia Gonzalez-Yebra
Ruben A. Rodriguez Rojas
Andrea Martínez-Pérez
Elder de la Rosa

SPIE.

Labeling of HeLa cells using $ZrO_2:Yb^{3+}$-Er^{3+} nanoparticles with upconversion emission

Andrea Ceja-Fdez,[a] Tzarara López-Luke,[a,*] Jorge Oliva,[a] Juan Vivero-Escoto,[b] Ana Lilia Gonzalez-Yebra,[c] Ruben A. Rodriguez Rojas,[d] Andrea Martínez-Pérez,[a,d] and Elder de la Rosa[a]

[a]Centro de Investigaciones en Óptica, A.C., Loma del Bosque 115, Lomas del Campestre, CP 37150, León, Guanajuato, México
[b]University of North Carolina at Charlotte, Department of Chemistry, 9201 University City Boulevard, Charlotte, North Carolina 28223, United States
[c]Universidad de Guanajuato Campus León, Departamento de Medicina y Nutrición, División Ciencias de la Salud, Boulevard Puente Milenio 1001, Predio San Carlos, CP 37670, León, Guanajuato, México
[d]Universidad de Guadalajara, Centro Universitario de los Lagos, Paseos de la Montaña, CP 47460, Lagos de Moreno, Jalisco, México

Abstract. This work reports the synthesis, structural characterization, and optical properties of $ZrO_2:Yb^{3+}$-Er^{3+} (2–1 mol%) nanocrystals. The nanoparticles were coated with 3-aminopropyl triethoxysilane (APTES) and further modified with biomolecules, such as Biotin-Anti-rabbit (mouse IgG) and rabbit antibody-AntiKi-67, through a conjugation method. The conjugation was successfully confirmed by Fourier transform infrared, zeta potential, and dynamic light scattering. The internalization of the conjugated nanoparticles in human cervical cancer (HeLa) cells was followed by two-photon confocal microscopy. The $ZrO_2:Yb^{3+}$-Er^{3+} nanocrystals exhibited strong red emission under 970-nm excitation. Moreover, the luminescence change due to the addition of APTES molecules and biomolecules on the nanocrystals was also studied. These results demonstrate that $ZrO_2:Yb^{3+}$-Er^{3+} nanocrystals can be successfully functionalized with biomolecules to develop platforms for biolabeling and bioimaging. [DOI: 10.1117/1.JBO.20.4.046006]

Keywords: photoluminescence; HeLa cells; Raman spectroscopy; zeta potential; dynamic light scattering; two-photon confocal microscopy.

Paper 140712R received Oct. 30, 2014; accepted for publication Mar. 16, 2015; published online Apr. 16, 2015.

1 Introduction

Lanthanide-doped nanomaterials are promising platforms for bioapplications due to their ability to convert low-energy near-infrared (NIR) radiation into higher-energy visible luminescence through a process called upconversion (UPC).[1,2] There are several potential benefits for the use of nanocrystals with UPC emission in biological applications, such as no damage of tissues; anti-Stokes emission; long lifetimes; photostability; increased contrast in biological specimens due to the absence of autofluorescence upon excitation with IR light; and simultaneous detection of multiple targeted analytes.[3–6] Other advantages of the UPC emission are the reduction of photobleaching and scattering in tissues, which avoid the use of complicated and high-cost femtosecond lasers and photomultiplier tubes.[7–10]

For biomedical applications, such as cancer detection, biolabeling, and bioimaging, luminescent nanoparticles preferably have to form a stable colloidal solution under physiological conditions. However, common nanomaterials with strong UPC emission, such as Yb^{3+}-Er^{3+} co-doped Y_2O_2S, Yb^{3+}-Ho^{3+} co-doped Y_2O_3, and Yb^{3+}-Er^{3+}-Tm^{3+} doped $NaYF_4$, are hydrophobic.[11–13] Some efforts have been made to convert hydrophobic UPC nanoparticles into hydrophilic ones using techniques such as polymer capping, surface silanization, and surface ligand oxidation.[13–18] Recent methods also include ligand exchange in $NaGdF_4:Ho^{3+}$-Yb^{3+} and $NaYF_4:Yb^{3+}$-Er^{3+} phosphors.[19]

Cancer detection in early stages is a priority for many medical groups around the world. In 2012, according to World Health Organization, cervical cancer was one of the most prevalent cancer types in the world. To detect and diagnose cancer, there are several biomarkers;[20–23] for example, the Ki-67 protein is expressed in all phases of the cell division cycle, but its expression level is strongly downregulated in the resting G0 phase. This characteristic makes the Ki-67 protein an excellent biomarker for cell proliferation.[24–26] This biomolecule can be used as a prognostic marker in many types of cancers.[27–31] Moreover, it has been demonstrated that cervical human cancer (HeLa) cells can be labeled using doped or undoped nanomaterials, such as $NaYF_4:Yb^{3+}$-Er^{3+}, $NaYF_4:Yb^{3+}$-Er^{3+}@CaF_2 core@-shell, $NaGdF_4:Yb^{3+}$-Er^{3+}/Silica/Au, CaF_2 and carbon nanoparticles. These nanomaterials were internalized in HeLa cells observing visible light from the nanoparticles under IR excitation.[32–36] Though these platforms are efficient for labeling HeLa cells, they still show several problems related to the complexity of their fabrication. For example, the synthesis of $NaGdF_4:Yb^{3+}$, Er^{3+} nanoparticles have some drawbacks for biomedical applications; therefore, gold or silica need to be used to render them with biocompatible properties.[37–39] In addition, one of the problems with carbon nanoparticles is the fact that they need to be excited with near-UV light, which can damage tissues around the cancer cells.[34]

Rare earth doped zirconia (ZrO_2) nanophosphors present efficient emission in the visible region when they are under IR excitation.[40–42] The ZrO_2 low phonon energy (470 cm^{-1}) increases the number and the probability of radiative transitions

*Address all correspondence to: Tzarara López-Luke, E-mail: tzarara@cio.mx

in rare earth doped ZrO_2.[43] Strong UPC emission has been obtained by doping ZrO_2 with different pairs of rare earths, such as Yb^{3+}-Tm^{3+}, Yb-Ho^{3+}, Er^{3+}, and Yb^{3+}-Er^{3+}.[44] Furthermore, ZrO_2 nanophosphors can be synthesized by low-cost methods, such as sol-gel,[45,46] sol-emulsion-gel,[47,48] spray pyrolysis,[49,50] and precipitation.[51] Interestingly, ZrO_2 is a nontoxic material; it has been used as a biocompatible dental material to make pigments.[52–55] Due to all of those reasons, ZrO_2 is an excellent candidate for developing novel biolabeling and bioimaging platforms. In this work, $ZrO_2:Yb^{3+}$-Er^{3+} nanocrystals were chemically conjugated with an antiKi-67 protein by a novel method using (3-aminopropyl)triethoxysilane (APTES) and conjugated Biotin molecules as ligands. To the best of our knowledge, there are no reports about the use of luminescent $ZrO_2:Yb^{3+}$, Er^{3+} nanocrystals to label HeLa cells. Furthermore, the effect of the ligands on the luminescent properties of these nanoparticles was studied. In addition, the internalization of the conjugated nanoparticles in HeLa cells was followed by looking at their strong red luminescence using two-photon confocal microscopy. The results show the successful uptake of conjugated $ZrO_2:Yb^{3+}$-Er^{3+} nanoparticles in HeLa cells. We envision that this is a promising method for labeling different types of cancer cells for biosensing and bioimaging purposes.

2 Experimental

2.1 *Preparation of* $ZrO_2:Yb^{3+}$-Er^{3+} *Nanoparticles*

$ZrO_2:Yb^{3+}$-Er^{3+} nanoparticles were prepared following a precipitation process previously reported with some modifications.[56] $ZrOCl_2 \cdot 8H_2O$ and $YbCl_3 \cdot 6H_2O$ (99.9%) were purchased from Aldrich, and $ErCl_3 \cdot 6H_2O$ (99.99%) was acquired from RE Acton. Ammonium hydroxide (NH_4OH) at 30 vol% was supplied by Karal. In a typical experiment, Yb^{3+}-Er^{3+} co-doped ZrO_2 with a molar ratio of 2:1 for $Yb^{3+}:Er^{3+}$ was prepared by dissolving 2.6333 g of $ZrOCl_2$, 0.2362 g of $YbCl_3 \cdot 6H_2O$ (2 mol % of Yb_2O_3), and 0.1351 g of $ErCl_3 \cdot 6H_2O$ (1 mol % of Er_2O_3) in 50 ml of a mixture of $H_2O/EtOH$ (1:1 wt%). After 15 min under stirring, the nonionic surfactant Pluronic F127 was introduced in the mixture at a molar ratio of $F127/ZrO_2 = 0.0082$. Afterward, 30 ml of NH_4OH was added to precipitate the salts. The resulted suspensions were transferred into a sealed autoclave and a hydrothermal treatment was carried out at 80°C for 12 h. After this, the autoclave was allowed to cool down for 30 min and the solutions were washed twice with absolute ethanol and water in a centrifuge at 4000 rpm for 10 min. Subsequently, the powders were put in a ceramic crucible and dried at 80°C for 12 h. Finally, all samples were annealed at 1000°C using a heating rate of 5°C/ min.

2.2 *Conjugation and Functionalization of* $ZrO_2:Yb^{3+}$-Er^{3+} *Nanoparticles*

The conjugation of $ZrO_2:Yb^{3+}$-Er^{3+} nanoparticles with the Ki-67 protein was carried out by following a previously reported method with some modifications.[15] This process was performed as follows: 0.1 g of Yb^{3+}-Er^{3+} doped ZrO_2 nanoparticles were stirred with 490 μl of APTES for 24 hours. This bifunctional compound has amine- and alkoxysilane groups. The alkoxysilane reacts with the OH moieties on the $ZrO_2:Yb^{3+}$-Er^{3+} nanoparticles surface, leaving the amino groups exposed for further functionalization. The samples were washed once with ethanol and water to eliminate the excess of residues and centrifuged at 6000 rpm for 10 min. The samples were dried at 40°C for 12 h. The Yb^{3+}-Er^{3+} co-doped ZrO_2 nanoparticles coated with APTES were dispersed in 670 μl of phosphate buffered saline (PBS) 1× (pH = 7.4) and then 200 μl of 1:500 Biotin-Anti-rabbit (mouse IgG) from BIOCARE was added to the suspension to bind the carboxylic acid groups of the IgG with the amino groups exposed in the nanoparticles; this suspension was kept at 4°C for 12 h. After that, the nanoparticles were washed with distilled water and centrifuged at 6000 rpm for 10 min to remove the supernatant. The conjugated material was kept at 37°C for 12 h. Subsequently, 300 μl of PBS 1× and 10 μl of antigen Ki-67-rabbit antibody from BIOCARE were added to the nanoparticles and stored for another 12 h at 4°C. Finally, the conjugated $ZrO_2:Yb^{3+}$-Er^{3+} nanoparticles were washed with distilled water and centrifuged at 6000 rpm for 10 min. The final material was dispersed and stored in distilled water.

2.3 *Structural Characterization (X-Ray Diffraction, Raman, HRTEM, SEM, Fourier Transform Infrared)*

X-ray diffraction (XRD) patterns were obtained using a SIEMENS D-5005 equipment using a Cu tube with Kα radiation at 1.5405 Å, scanning in the 20 to 80 deg 2θ range with increments of 0.02 deg and a sweep time of 2 s. Raman patterns were obtained using a Renishaw Raman System (inVia Raman Microscope), which uses a 785-nm laser and a 50× objective. The nanoparticles were suspended in isopropyl alcohol at room temperature and dispersed with ultrasonication. Afterward, the solution of nanoparticles was dropped on 3-mm-diameter lacey carbon copper grids to obtain the HRTEM images in an FEI Titan 80-300 with an accelerating voltage set to 300 kV. In addition, the nanoparticle micrographs were obtained by an SEM Hitachi SU8010 at 30.0 kV. The Fourier transform infrared (FTIR) spectra were obtained using a Perkin-Elmer spectrophotometer with a deuterated triglycine sulfate detector and a spectral resolution of 4 cm^{-1}. The samples were prepared using the KBr pellet method and the spectra were obtained in the range of 1000 to 4000 cm^{-1}.

2.4 *Photoluminescence Characterization*

Photoluminescence characterization was performed using a continuous wave semiconductor laser diode with an excitation power of 350 mW and centered at 970 nm. The luminescence emission was analyzed with a Spectrograph Spectra Pro 2300i and a R955 photomultiplier tube from Hamamatsu. The system was PC controlled with Spectra Sense software. The samples were supported in 1 mm capillary tubes in order to guarantee the same quantity of excited material. Special care was taken to maintain the alignment of the setup in order to compare the intensities between different characterized samples. All measurements were performed at room temperature.

2.5 *Incubation and Confocal Microscopy*

HeLa cells were grown at a density of 5×10^4 cells/mL in six-well culture plates with coverslips at the bottom and incubated in 3 mL of RPMI-1640 cell media for 24 h at 37°C under 5% CO_2. After this, the cell media was replaced by 3 ml of $ZrO_2:Yb^{3+}$-Er^{3+} nanoparticles, $ZrO_2:Yb^{3+}$-Er^{3+}-APTES, and $ZrO_2:Yb^{3+}$-Er^{3+}-APTES-Biotin-Anti-rabbit/rabbit antibody-AntiKi-67

with a concentration of 100 μg/mL and was incubated for 6 h. Finally, the cell-plated coverslips corresponding to each sample were washed twice with PBS buffer (1 mM, pH 7.4) and stained with nuclei-staining NucBlue® Live solution for 15 min. All the cell-plated coverslips were fixed with a solution of 4% formaldehyde. The fixed and stained coverslips were placed in microscope slides and analyzed under a two-photon Olympus FV1000 MPE SIM laser scanning confocal microscope.

2.6 *Zeta Potential and Dynamic Light Scattering Measurements*

Dynamic light scattering (DLS) and zeta potential measurements were carried out using a Malvern Instrument Zetasizer Nano (red laser 633 nm). The samples were dispersed in PBS (1 mM, pH = 7.4) with a concentration of 1 mg/mL. The DLS and zeta potential were analyzed at 25°C.

3 Results and Discussion

3.1 *Crystalline Structure and Morphology*

The XRD pattern of the $ZrO_2:Yb^{3+}$-Er^{3+} nanopowder is shown in Fig. 1(a). This plot shows peaks corresponding to (1,0,1), (0,1,1), (2,1,1), and (1,1,2) planes, respectively. All the peaks are associated with the tetragonal phase of zirconia, according to the JCPDS 37-1413 card.[57] The $ZrO_2:Yb^{3+}$-Er^{3+} nanopowder obtained by the precipitation method was analyzed by Raman spectroscopy, see Fig. 1(b). The peaks at 626, 552, 525, 445, 336, 260, 238, and 185 cm^{-1} represent the spectrum. The peaks located at 445 and 626 cm^{-1} as well as the shoulders located at 185 and 260 cm^{-1} are in agreement with the tetragonal phase of zirconia.[58] The nanocrystal sizes were determined by TEM and a representative micrograph is presented in Fig. 2(a). The nanocrystals have an average size of 20 nm and spherical shape. Besides, Fig. 2(b) is an SEM image, which shows well-dispersed nanocrystals, and this was caused by the introduction of PF127 during the synthesis process.[59] The size and dispersion of the co-doped $ZrO_2:Yb^{3+}$-Er^{3+} nanocrystals was controlled from the nucleation process due to the presence of ammonia, water/ethanol, and surfactant Pluronic PF127.[56] To promote the efficient internalization in HeLa cells, it is important to have particles in the nanoscale size regime. In addition, the colloidal stability of the nanoparticles is also significant to avoid the formation of aggregates, which may prevent the effective interaction between the nanoparticles and the cell surface.

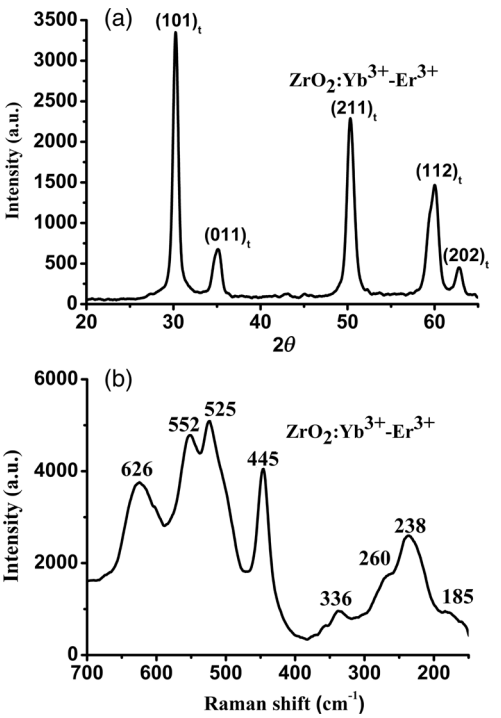

Fig. 1 Structural characterization of $ZrO_2:Yb^{3+}$-Er^{3+} nanocrystals: (a) x-ray diffraction and (b) Raman spectroscopy, using a laser of 785 nm.

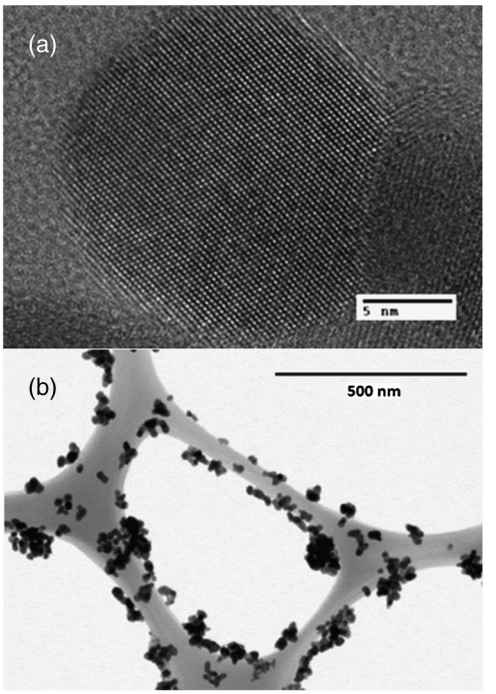

Fig. 2 (a) HRTEM image and (b) SEM image of $ZrO_2:Yb^{3+}$-Er^{3+} nanoparticles.

3.2 *FTIR, Zeta-Potential, and DLS*

Figure 3 shows the FTIR spectra of $ZrO_2:Yb^{3+}$-Er^{3+} nanocrystals and $ZrO_2:Yb^{3+}$-Er^{3+} prepared with APTES, Biotin-Anti-rabbit (mouse IgG), and rabbit antibody-AntiKi-67, respectively. These spectra provide information regarding functional groups and impurities on the surface of nanoparticles. They also corroborated that the process of functionalization and conjugation was successfully achieved. Figure 3(a) shows the FTIR spectra of nonfunctionalized nanoparticles $ZrO_2:Yb^{3+}$-Er^{3+}. It depicts small peaks associated with OH groups in the range of 3200 to 3600 cm^{-1}. Moreover, a peak is also observed at 450 cm^{-1}, which is related to the Zr—O stretching vibrations.[60] The spectrum in Fig. 3(b) shows a broadening of the bands centered at 3600 and 564 cm^{-1} due to the presence of Si—OH and Si—O—Si bonds, respectively.[61,62] Other peaks at ~2923 and 2351 cm^{-1} are related to C—H bonds and CO_2 impurities, respectively. The band located in the range of 3000 to 3400 cm^{-1} is associated with amine groups.[63,64] The CO_2 impurities adsorbed in the surface of the nanoparticles can come from the synthesis and/or the environment during the

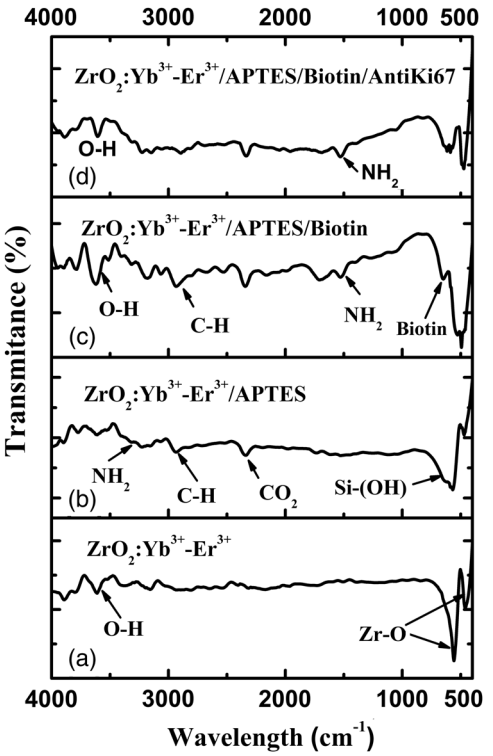

Fig. 3 Fourier transform infrared spectra of (a) $ZrO_2:Yb^{3+}$-Er^{3+}, (b) $ZrO_2:Yb^{3+}$-Er^{3+}/(3-aminopropyl)triethoxysilane (APTES), (c) $ZrO_2:Yb^{3+}$-Er^{3+}/APTES/Biotin, and (d) $ZrO_2:Yb^{3+}$-Er^{3+}/APTES/Biotin/AntiKi67.

measurement process, which was probably caused by the granular characteristic of the nanopowder. The OH groups were introduced during the hydrolysis and condensation process where the M-OH (M = Zr, Er, and Yb) bond was formed due to the excess of hydroxyls in solution. According to the FTIR spectra in Figs. 3(a) and 3(b), the contamination produced by those hydroxyl groups is very low. Biotin-Anti-rabbit (mouse IgG) protein is conjugated to the nanoparticles containing APTES by forming an amide bond between the free amino groups located at the surface of $ZrO_2:Yb^{3+}$-Er^{3+}/APTES and the carboxylic acid groups exposed in the IgG protein. The $ZrO_2:Yb^{3+}$-Er^{3+}/APTES/Biotin FTIR spectrum is shown in Fig. 3(c); the spectrum illustrates a new band associated with the amide bond at 1770 cm^{-1}. Moreover, a peak centered at 658 cm^{-1} is also associated with Biotin according to literature.[65,66] These data further confirm the functionalization of nanoparticles. The next step is to analyze the process of conjugation with the antigen Ki-67-rabbit antibody ($ZrO_2:Yb^{3+}$-Er^{3+}/APTES/Biotin/AntiKi-67), see Fig. 3(d). The bands related to Biotin are still observed, and there is a general decrease of the peaks related to impurities such as CO_2 and OH radicals. However, it is observed that there is a widening of the 658 cm^{-1} band when AntiKi-67 is added. Based on this information, it is expected that AntiKi-67 is readily available to interact with HeLa cells.

The conjugation of the nanoparticles was also analyzed by zeta potential and DLS measurements, see Table 1. The zeta potential changed from negative to positive when the $ZrO_2:Yb^{3+}$-Er^{3+} nanoparticles surface is modified with APTES, which is an indication that the amino groups are covering the nanoparticles surface. Moreover, the zeta potential was shifted from positive to negative after Biotin and antigen Ki-67 proteins

Table 1 Nanoparticle characterization using dynamic light scattering (DLS) and zeta potential for $ZrO_2:Yb^{3+}$-Er^{3+}, $ZrO_2:Yb^{3+}$-Er^{3+}-(3-aminopropyl)triethoxysilane (APTES), and $ZrO_2:Yb^{3+}$-Er^{3+}-APTES-Biotin-AntiKi67 nanocrystals.

	$ZrO_2:Yb^{3+}$-Er^{3+}	$ZrO_2:Yb^{3+}$-Er^{3+}-APTES	$ZrO_2:Yb^{3+}$-Er^{3+}-APTES-Biotin-AntiKi67
DLS (*d*, nm)	748	1232	4694
Zeta potential (mV)	−36.8	+10.8	−36.0

were chemically attached to the surface of the material, suggesting the presence of carboxylate groups.[67,68] A value of −36 mV obtained in $ZrO_2:Yb^{3+}$-Er^{3+}/APTES/Biotin/AntiKi-67 also indicates that nanoparticles can be stable in PBS due to their high electrostatic repulsion, which is suitable for bioapplications. A high negative value also suggests a high adsorption of nanoparticles on the nucleus of HeLa cells.[69] Moreover, DLS measurements showed that the hydrodynamic diameter of the nanoparticles increased when the different molecules were added; the average sizes for $ZrO_2:Yb^{3+}$-Er^{3+}, $ZrO_2:Yb^{3+}$-Er^{3+}/APTES, and $ZrO_2:Yb^{3+}$-Er^{3+}/APTES/Biotin/AntiKi-67 were 748, 1232, and 4694 nm, see Table 1. The size of the nanoparticles in $ZrO_2:Yb^{3+}$-Er^{3+} does not coincide with the one measured with TEM, probably due to the agglomeration of nanoparticles that were dispersed in PBS.

Figure 4 shows a schematic representation for the functionalization and conjugation of the nanoparticles. The OH moieties produced after $ZrO_2:Yb^{3+}$-Er^{3+} synthesis react with the alkoxysilane groups of APTES to afford a silica shell on the nanoparticles leaving the amine groups exposed on the surface of the material. In the next step of the reaction, the Biotin-Anti-rabbit (mouse IgG) molecule is conjugated to the amino groups by using the COOH moieties of the IgG. At this point, the Anti-rabbit can interact with the biomolecule AntiKi-67-rabbit antibody.

3.3 *Luminescent Properties*

The mechanism of UPC emission in Er^{3+}-Yb^{3+} co-doped ZrO_2 is well established in the literature.[70] Figure 5 shows a strong red emission band with peaks at 653 and 657 nm as well as a weak green band after excitation at 970 nm. Green and red emission bands are assigned to $^2H_{11/2} + {}^4S_{3/2} \rightarrow {}^4I_{15/2}$ and $^4F_{9/2} \rightarrow {}^4I_{15/2}$ transitions of the Er^{3+} ion, and they are caused by the successive absorption of two photons after energy transfer from Yb^{3+} ions.[59] According to previous works, the emission is predominantly red because OH groups have a vibrational energy (3000 to 4000 cm^{-1}) which produces nonradiative relaxations from the mixed level $^2H_{11/2} + {}^4S_{3/2}$ toward the $^4F_{9/2}$ level.[71] In our case, the presence of OH moieties in all samples is corroborated by the FTIR spectra in Fig. 3. The inset in Fig. 5 shows that the integrated emission corresponds to the red band. Moreover, it is observed that the red emission of the samples $ZrO_2:Yb^{3+}$-Er^{3+}/APTES (Z-A) and $ZrO_2:Yb^{3+}$-Er^{3+}/APTES/Biotin (Z-A-B) decreases progressively with respect to the sample of reference without conjugated ($ZrO_2:Yb^{3+}$-Er^{3+}) (Z). Nevertheless, the emission was improved when the

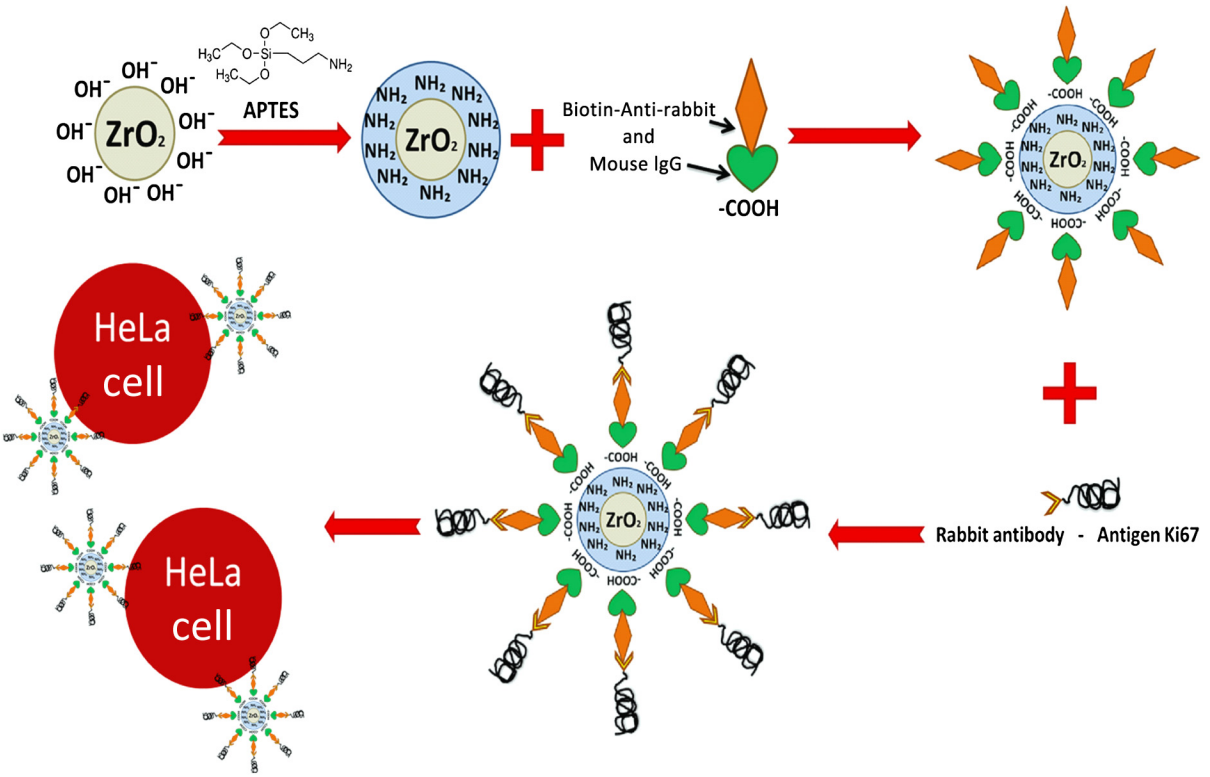

Fig. 4 Schematic representation of the functionalization and conjugation of $ZrO_2:Yb^{3+}$-Er^{3+} nanoparticles.

nanoparticles were conjugated with AntiKi-67 (APTES-Biotin-AntiKi-67) (Z-A-B-K). The integrated red emission diminished with the addition of APTES and Biotin molecules because other contaminants, such as CO_2, C—H, and amine groups, appeared and the presence of hydroxyls increased. These elements may act as quenching centers of luminescence and also create defects, which behave as traps for luminescence.[71,72] It is important to point out that the sample with APTES-Biotin had the highest levels of impurities [see Fig. 3(c)]; therefore, it showed the lowest luminescence. In contrast, the sample with APTES-Biotin-AntiKi-67 had the lowest amount of contaminants (OH, CO_2, and C—H) [see Fig. 3(d)]; therefore, it presented the highest red emission, see Fig. 5.

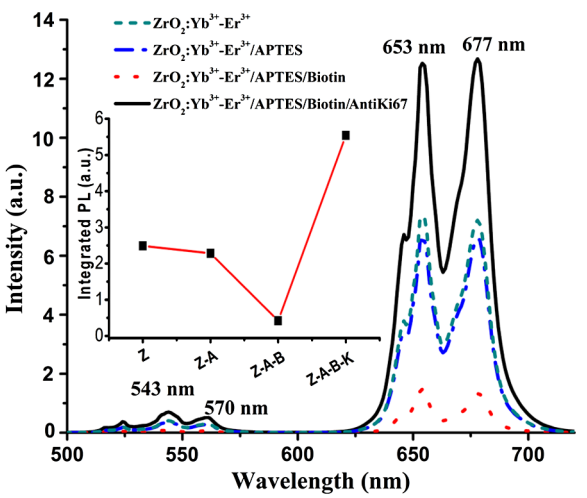

Fig. 5 Photoluminescence spectra of $ZrO_2:Yb^{3+}$-Er^{3+}, $ZrO_2:Yb^{3+}$-Er^{3+}/APTES, $ZrO_2:Yb^{3+}$-Er^{3+}/APTES/Biotin, and $ZrO_2:Yb^{3+}$-Er^{3+}/APTES/Biotin/AntiKi67. Inset shows the integrated emission of the samples.

3.4 *Imaging of* $ZrO_2:Yb$-Er *Nanocrystals Incubated in HeLa Cells*

Figure 6 shows the images obtained by the two-photon confocal microscope after HeLa cells were incubated with the different materials synthesized in this work. Figure 6(a) shows that the $ZrO_2:Yb^{3+}$-Er^{3+} nanoparticles are situated out of the cell, probably due to the negative charge on the surface of the nanoparticles, which limits the internalization in HeLa cells. Figure 6(b) depicts $ZrO_2:Yb^{3+}$-Er^{3+}/APTES nanoparticles located on the cytoplasm of HeLa cells; these nanoparticles have no AntiKi-67, but they have APTES on their surface; this indicates that the positive charge on the surface of the nanoparticles enhances the internalization in HeLa cells. Figure 6(c) is an image of HeLa cells with nanoparticles conjugated with AntiKi-67; it is observed that 6 h of incubation is sufficient to reach the cytoplasm of HeLa cells. It is observed that there are a greater number of particles within the cell and near the nucleus. The most accepted theory is that nanoparticles are internalized via endosome-mediated transport or through ribosome exchanges.[33] In general, the red emission from nanoparticles is strong in all images, which demonstrates the efficient luminescence generated by the nanoparticles synthesized in this work. It is worth noting that there was no autofluorescence from the cells after exciting the UPC nanoparticles with 970 nm. Furthermore, these images denote different sizes of emission points; this is probably induced by the nanoparticle agglomeration.

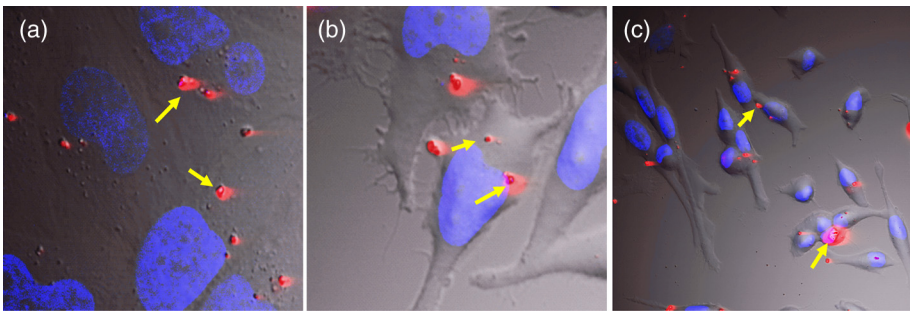

Fig. 6 Confocal microscopy images of (a) $ZrO_2:Yb^{3+}$-Er^{3+}, (b) $ZrO_2:Yb^{3+}$-Er^{3+}/APTES, (c) $ZrO_2:Yb^{3+}$-Er^{3+}/APTES/Biotin/AntiKi67 nanoparticles after 6 h of incubation in HeLa cells.

Compared to other methods for the conjugation of nanoparticles, our technique avoids the use of other elements, such as carbon and citrate, which are relatively toxic.[32,34] Moreover, it uses biomolecules (antigen and antibody) to lead our nanoparticle toward a targeted organelle; to the best of our knowledge, this kind of molecule has not been used on luminescent nanoparticles. Finally, further research is needed not only to improve the distribution and internalization of nanoparticles, but also to label specific organelles inside the HeLa cells. Those studies are in progress, and they will be presented in a subsequent work.

4 Conclusions

In summary, we conjugated Yb^{3+}-Er^{3+} co-doped ZrO_2 nanoparticles using Biotin-Anti-rabbit (mouse IgG) and rabbit antibody-AntiKi-67 biomolecules. The successful conjugation was confirmed by FTIR, zeta potential, and DLS. The nanoparticles internalized in HeLa cells demonstrated a strong red luminescence and were observed using a two-photon confocal microscope. The photoluminescence spectra indicated that the UPC red emission of Er^{3+} ions is affected by the molecules located on the nanocrystals' surface. An enhancement of the red emission was obtained in the nanoparticles with the conjugation with AntiKi-67. This was mainly caused by an enormous reduction of impurities compared to the rest of the samples. Our results indicate that the method of conjugation depicted in this work can be a promising alternative to afford stable colloidal dispersions of nanoparticles in water and efficiently label cancer cells.

Acknowledgments

We acknowledge the financial support from CONACyT through research grant 134111 and a PhD scholarship for Andrea Ceja. Dr. J.V.-E. thanks the start-up support from UNC-Charlotte. We also acknowledge Dr. Richard Jew for critical reading of the manuscript and helpful suggestions.

References

1. X. M. Li, F. Zhang, and D. Y. Zhao, "Highly efficient lanthanide upconverting nanomaterials: progresses and challenges," *Nano Today* **8**(6), 643–676 (2013).
2. F. Wang and X. G. Liu, "Multicolor tuning of lanthanide-doped nanoparticles by single wavelength excitation," *Acc. Chem. Res.* **47**(4), 1378–1385 (2014).
3. L. C. Ong et al., "Bacterial imaging with photostable upconversion fluorescent nanoparticles," *Biomaterials* **35**(9), 2987–2998 (2014).
4. F. Chen et al., "Functionalized upconversion nanoparticles: versatile nanoplatforms for translational research," *Curr. Mol. Med.* **13**(10), 1613–1632 (2013).
5. Y. H. Chien et al., "Near-infrared light photocontrolled targeting, bioimaging, and chemotherapy with caged upconversion nanoparticles in vitro and in vivo," *ACS Nano* **7**(10), 8516–8528 (2013).
6. B. G. Yust, F. J. Pedraza, and D. K. Sardar, "Ultrasmall lanthanide-doped nanoparticles as multimodal platforms, *Proc. SPIE* **8956**, 895608 (2014).
7. D. Y. Li et al., *Multifunctional Y2O3:Yb3+/Tm3+/Li+ Nanocrystals with Enhanced Near-Infrared to Near-Infrared Upconversion Photoluminescence*, Trans Tech Publications Ltd, Stafa-Zurich (2011).
8. Z. Liu et al., "Near-infrared lanthanide luminescence for functional materials," *Prog. Chem.* **23**(1), 153–164 (2011).
9. T. Liu et al., "Rare-earth upconversion nanophosphors," *Prog. Chem.* **24**(2–3), 304–317 (2012).
10. C. F. Gainer and M. Romanowski, "A review of synthetic methods for the production of upconverting lanthanide nanoparticles," *J. Innov. Opt. Health Sci.* **7**(2), 11 (2014).
11. B. C. Hwang et al., "Cooperative upconversion and energy transfer of new high Er^{3+}- and Yb^{3+}-Er^{3+}-doped phosphate glasses," *J. Opt. Soc. Am. B Opt. Phys.* **17**(5), 833–839 (2000).
12. R. S. Meltzer et al., "Effect of the matrix on the radiative lifetimes of rare earth doped nanoparticles embedded in matrices," *J. Lumin.* **94**, 217–220 (2001).
13. T. Zako et al., "Development of near infrared-fluorescent nanophosphors and applications for cancer diagnosis and therapy," *J. Nanomater.* **2010**, 491471 (2010).
14. J. Aldana, Y. A. Wang, and X. G. Peng, "Photochemical instability of CdSe nanocrystals coated by hydrophilic thiols," *J. Am. Chem. Soc.* **123**(36), 8844–8850 (2001).
15. P. L. A. M. Corstjens et al., "Infrared up-converting phosphors for bioassays," *IEE Proc. Nanobiotechnol.* **152**(2), 64–72 (2005).
16. H. Kwon et al., "Synthesis and characterization of poly(vinylpyrrolidone)-capped silicon-nanoparticles," *J. Nanosci. Nanotechnol.* **14**(8), 5983–5987 (2014).
17. C. R. Wade et al., "Postsynthetic tuning of hydrophilicity in pyrazolate MOFs to modulate water adsorption properties," *Energy Environ. Sci.* **6**(7), 2172–2177 (2013).
18. K. Wei, X. M. Peng, and F. Zou, "Folate-decorated PEG-PLGA nanoparticles with silica shells for capecitabine controlled and targeted delivery," *Int. J. Pharm.* **464**(1–2), 225–233 (2014).
19. Q. B. Zhang et al., "$NaYF_4:Yb^{3+}$, Er^{3+} upconverting nanoparticles surface ligand exchange in ternary mixture solvent and optical properties," *Chem. J. Chin. Univ.* **35**(2), 224–229 (2014).
20. C. M. M. Amaral et al., "MDM2 polymorphism associated with the development of cervical lesions in women infected with human papillomavirus and using of oral contraceptives," *Infect. Agent Cancer* **9**, 24 (2014).
21. G. B. Park et al., "Antibody ligation of CM1 on cisplatin-exposed Hela cells induces apoptosis through reactive oxygen species-dependent Fas ligand expression," *Int. J. Oncol.* **44**(6), 2016–2024 (2014).
22. F. Guerra et al., "Argentophilic nucleolus organizer region as a proliferation marker in cervical intraepithelial neoplasia grade 1 of the uterine cervix," *J. Obstet. Gynaecol. Res.* **40**(6), 1717–1724 (2014).
23. K. K. L. Samaga et al., "Synthetic racemates of abyssinone I and II induces apoptosis through mitochondrial pathway in human cervix carcinoma cells," *Bioorg. Chem.* **56**, 54–61 (2014).

24. J. Bullwinkel et al., "Ki-67 protein is associated with ribosomal RNA transcription in quiescent and proliferating cells," *J. Cell. Physiol.* **206**(3), 624–635 (2006).
25. J. Gerdes et al., "Cell-cycle analysis of a cell proliferation-associated human nuclear antigen defined by the monoclonal-antibody Ki-67," *J. Immunol.* **133**(4), 1710–1715 (1984).
26. J. Gerdes et al., "Production of a mouse monoclonal-antibody reactive with a human nuclear antigen associated with cell-proliferation," *Int. J. Cancer* **31**(1), 13–20 (1983).
27. J. Bulten et al., "MIB1, a promising marker for the classification of cervical intraepithelial neoplasia," *J. Pathol.* **178**(3), 268–273 (1996).
28. D. W. Chan et al., "Over-expression of FOXM1 transcription factor is associated with cervical cancer progression and pathogenesis," *J. Pathol.* **215**(3), 245–252 (2008).
29. A. J. Kruse et al., "Ki-67 immunoquantitation in cervical intraepithelial neoplasia (CIN): a sensitive marker for grading," *J. Pathol.* **193**(1), 48–54 (2001).
30. S. Lobato et al., "Minichromosome maintenance 7 protein is a reliable biological marker for human cervical progressive disease," *J. Gynecol. Oncol.* **23**(1), 11–15 (2012).
31. M. Takagi et al., "Ki67 antigen contributes to the timely accumulation of protein phosphatase 1 gamma on anaphase chromosomes," *J. Biol. Chem.* **289**(33), 22877–22887 (2014).
32. T. Y. Cao et al., "Water-soluble $NaYF_4$:Yb/Er upconversion nanophosphors: synthesis, characteristics and application in bioimaging," *Inorg. Chem. Commun.* **13**(3), 392–394 (2010).
33. B. Sikora et al., "Transport of $NaYF_4$:Er^{3+}, Yb^{3+} up-converting nanoparticles into HeLa cells," *Nanotechnology* **24**(23), 11 (2013).
34. S. K. Bhunia et al., "Carbon nanoparticle-based fluorescent bioimaging probes," *Sci. Rep.* **3**, 1473 (2013).
35. Y.-F. Wang et al., "Rare-earth nanoparticles with enhanced upconversion emission and suppressed rare-earth-ion leakage," *Chem.* **18**(18), 5558B5564 (2012).
36. W. Yin et al., "Design of multifunctional alkali ion doped CaF_2 upconversion nanoparticles for simultaneous bioimaging and therapy," *Dalton Trans.* **43**(10), 3870 (2014).
37. J. C. Zhou et al., "Bioimaging and toxicity assessments of near-infrared upconversion luminescent $NaYF_4$:Yb, Tm nanocrystals," *Biomaterials* **32**(34), 9059–9067 (2011).
38. X. Wang et al., "One-step solvothermal synthesis of targetable optomagnetic upconversion nanoparticles for in vivo bimodal imaging," *Anal. Chem.* **85**(21), 10225–10231 (2013).
39. S. Shan et al., "Preparation and biological application of rare earth upconversion fluorescent nanomaterials," *Prog. Biochem. Biophys.* **40**(10), 925–934 (2013).
40. A. Patra et al., "Upconversion in Er^{3+}:ZrO_2 nanocrystals," *J. Phys. Chem. B* **106**(8), 1909–1912 (2002).
41. A. Patra et al., "Blue upconversion emission of Tm^{3+}-Yb^{3+} in Zro_2 nanocrystals: role of Yb^{3+} ions," *Chem. Phys. Lett.* **407**(4–6), 477–481 (2005).
42. A. Speghini et al., "Preparation, structural characterization, and luminescence properties of Eu^{3+}-doped nanocrystalline ZrO_2," *J. Mater. Res.* **20**(10), 2780–2791 (2005).
43. F. Gu et al., "Effect of Dy^{3+} doping and calcination on the luminescence of ZrO_2 nanoparticles," *Chem. Phys. Lett.* **380**(1–2), 185–189 (2003).
44. G. Y. Chen et al., "Upconversion mechanism for two-color emission in rare-earth-ion-doped Zro_2 nanocrystals," *Phys. Rev. B* **75**(19), 195204 (2007).
45. P. Salas et al., "High temperature thermoluminescence induced on UV-irradiated tetragonal ZrO_2 prepared by sol-gel," *Mater. Lett.* **45**(5), 241–245 (2000).
46. M. Stoia, P. Barvinschi, and F. Barvinschi, "Structural and morphologic characterization of zirconia-silica nanocomposites prepared by a modified sol-gel method," *J. Cryst. Growth* **401**, 462–468 (2014).
47. P. Ghosh and A. Patra, "Role of surface coating in ZrO_2/Eu^{3+} nanocrystals," *Langmuir* **22**(14), 6321–6327 (2006).
48. L. A. Gomez et al., "Upconversion in Er^{3+}-doped ZrO_2 nanocrystals pumped at 1.426 μm," *J. Appl. Phys.* **103**(5), 4 (2008).
49. A. Martinez-Hernandez et al., "Synthesis and cathodoluminescence characterization of ZrO_2:Er^{3+} films," *J. Lumin.* **153**, 140–143 (2014).
50. H. Torabmostaedi et al., "Process control for the synthesis of ZrO_2 nanoparticles using FSP at high production rate," *Powder Technol.* **246**, 419–433 (2013).
51. V. H. Romero et al., "Brilliant blue, green and orange-red emission band on Tm^{3+}-, Tb^{3+}- and Eu^{3+}-doped ZrO_2 nanocrystals," *J. Phys. D Appl. Phys.* **43**(46), 465105 (2010).
52. T. J. Brunner et al., "In vitro cytotoxicity of oxide nanoparticles: comparison to asbestos, silica, and the effect of particle solubility," *Environ. Sci. Technol.* **40**(14), 4381 (2006).
53. G. Karunakaran et al., "Impact of nano and bulk ZrO_2, TiO_2 particles on soil nutrient contents and PGPR," *J. Nanosci. Nanotechnol.* **13**(1), 678–685 (2013).
54. S. Kanchana and S. Hussain, "Zirconia a bio-inert implant material," *IOSR J. Dent. Med. Sci.* **12**(6), 66–67 (2013).
55. S. P. C. Sam, V. S. Prasad, and K. S. Kumar, "Novel nontoxic nanopigments based on zirconia and rare earth mixed oxides," *Cryst. Res. Technol.* **45**(11), 1203 (2010).
56. T. Lopez-Luke et al., "Solvent and surfactant effect on the self-assembly and luminescence properties of ZrO_2:Eu^{3+} nanoparticles," *Appl. Phys. B Lasers Opt.* **102**(3), 641–649 (2011).
57. W. Cordova-Martinez et al., "Nanocrystalline tetragonal zirconium oxide stabilization at low temperatures by using rare earth ions: Sm^{3+} and Tb^{3+}," *Opt. Mater.* **20**(4), 263–271 (2002).
58. B.-K. Kim, J.-W. Hahn, and K. Han, "Quantitative phase analysis in tetragonal-rich tetragonal/monoclinic two phase zirconia by Raman spectroscopy," *J. Mater. Sci. Lett.* **16**(8), 669–671 (1997).
59. T. Lopez-Luke et al., "Enhancing the up-conversion emission of ZrO_2:Er^{3+} nanocrystals prepared by a Micelle process," *J. Phys. Chem. C* **111**(45), 17110–17117 (2007).
60. J. H. Iko Hyppänen et al., "Upconversion properties of nanocrystalline ZrO_2:Yb^{3+}, Er^{3+} phosphors," *J. Nanomater.* **2007**, 16391 (2007).
61. L. C. D. Rajput et al., "Silica coating of polymer nanowires produced via nanoimprint lithography from femtosecond laser machined templates," *Nanotechnology* **23**(10), 105304 (2012).
62. Q. Zhang, J. Luo, and Y. Wei, "A silica gel supported dual acidic ionic liquid: an efficient and recyclable heterogeneous catalyst for the one-pot synthesis of amidoalkyl naphthols," *Green Chem.* **12**(12), 2254 (2010).
63. J. Pu et al., "Fabrication of novel graphene-fullerene hybrid lubricating films based on self-assembly for MEMS applications," *Chem. Commun.* **50**(4), 469–471 (2014).
64. Y. Xu et al., "A fluorescent sensor for zinc detection and removal based on core-shell functionalized Fe_3O_4@SiO_2 nanoparticles," *J. Nanomater.* **2013**, 178138 (2013).
65. A. A. Bunaciu et al., "FT-IR spectrophotometric analysis of ascorbic acid and Biotin and their pharmaceutical formulations," *Anal. Lett.* **42**(10), 1327 (2009).
66. G. A. Mahmud et al., "A comparative study of aminosilanes for the application of reproducible, ultralow detection of biomolecules," 2012, http://ma.ecsdl.org/content/MA2012-01/45/1630.full.pdf (20 March 2015).
67. Z. Li et al., "Modification of $NaYF_4$:Yb, Er@SiO_2 nanoparticles with gold nanocrystals for tunable green-to-red upconversion emissions," *J. Phys. Chem. C* **115**(8), 3296 (2011).
68. B. F. Pan et al., "Effects of carbon nanotubes on photoluminescence properties of quantum dots," *J. Phys. Chem. C* **112**(4), 939–944 (2008).
69. W. Lina et al., "Surface passivation of carbon nanoparticles with branched macromolecules influences near infrared bioimaging," *Theranostics* **3**(9), 677–686 (2013).
70. D. Solis et al., "Surfactant effect on the upconversion emission and decay time of Zro_2:Yb-Er nanocrystals," *J. Lumin.* **129**(5), 449–455 (2009).
71. T. Lopez-Luke et al., "Improving pure red upconversion emission of co-doped Y_2O_3:Yb^{3+}-Er^{3+} nanocrystals with a combination of sodium sulfide and surfactant pluronic-F127," *J. Lumin.* **145**, 292–298 (2014).
72. C. Landes et al., "Photoluminescence of CdSe nanoparticles in the presence of a hole acceptor: N-butylamine," *J. Phys. Chem. B* **105**(15), 2986 (2001).

Andrea Ceja-Fdez is a PhD student at Optics Research Center (Centro de Investigaciones en Optica A.C.). Her research is focused on the synthesis and optical characterization of metal and nonmetal nanoparticles. She also works in developing SERS substrates for low-detection applications of different molecules, such as glucose, or overexpressed proteins in human cells, which can be used for biolabeling, biomaging, and cancer detection.

Tzarara López-Luke is a researcher in Optics Research Center (Centro de Investigaciones en Óptica, A.C). The research is based on synthesis of luminescent metallic oxides (Rare earth doped ZrO_2, Y_2O_3, Y_2O_2S), semiconductors (CdSe, CdTe, TiO_2, $TiO_2:N$) and metal nanoparticles (Au and Ag) with special structures, morphologies and optical properties, for the study in cancer detection and therapy, low concentration of glucose detection, new sources of illumination, and solar energy conversion.

Jorge Oliva obtained his PhD in optics from the Centro de Investigaciones en Optica A.C. in 2014. His research covers the fabrication and design of hybrid light-emitting diodes and solar cells for industrial applications and lighting. He also does research to develop SERS substrates for ultralow detection of proteins. He is an expert in synthesizing rare earth doped nanophosphors.

Juan Vivero-Escoto was a Carolina Postdoctoral Program for Faculty Diversity fellow at the University of North Carolina–Chapel Hill, and he became an assistant professor of chemistry at the University of North Carolina–Charlotte in 2012. He received the Wells Fargo Faculty Excellence Award 2013 and Ralph E. Powe Junior Faculty Enhancements Award (2013–2014). He has published over 30 publications, including papers and book chapters. His research focuses on designing hybrid nanomaterials for biomedical applications.

Ana Lilia Gonzalez-Yebra received his bachelor in chemistry from the Faculty of Chemistry of the University of Guanajuato (1997), and masters (2002–2004) and doctor of medicine (2004–2006) oriented to toxicology from the Institute of Medical Sciences at University of Guanajuato. Since 2006, he is professor in the Division of Health Sciences at the University of Guanajuato. He develops research on toxicology studies focused on chemical identification of cell damage. He has five publications in international refereed journals.

Ruben A. Rodriguez Rojas received his BE degree in electronic engineering from Technological Institute of Celaya and ME degree from Guanajuato University in electronics in 1998 and 2000, respectively. He also received his PhD in optics from the Center for Research in Optics (CIO) in 2004. He is actually a researcher in the Department of Exact and Technology of the University of Guadalajara since 2004. His interests are in optical materials and nanotechnology for lighting, solar cells, and biomedical applications.

Andrea Martínez-Pérez is a graduate student in biochemical engineering at the Guadalajara University in collaboration with the Optics Research Center (Centro de Investigaciones en Optica A.C.). Her thesis work was based on synthetized luminescent oxides and their bioconjugation.

Elder de la Rosa is the director of Optics Research Center (Centro de Investigaciones en Optica A.C.). His research interests are in linear and nonlinear optical properties of advanced materials for photonic applications, synthesis and characterization of nanostructured luminescent materials (oxides, semiconductors, metals) for lighting, solar cells and biomedical applications, preparation and characterization of soft glass luminescence (P2O5, TeO2) rare earth doped lasers, and fiber amplifiers.